AIAA JOURNAL
Vol. 44, No. 2, February 2006

Direct Numerical Simulation of Turbulent Flow Separation from a Wall-Mounted Hump

Dieter Postl* and Hermann F. Fasel†
University of Arizona, Tucson, Arizona 85721

A high-order-accurate numerical method for solving the incompressible Navier–Stokes equations in general orthogonal coordinates is presented. The method is applied to a test case of the NASA Langley Computational Fluid Dynamics Validation Workshop 2004, a turbulent flow over a wall-mounted hump geometry. Results of direct numerical simulations (DNS) for the unforced flow as well as for a case with steady suction are presented and compared to the available experimental data. The DNS predictions are shown to agree well with the experiments, except in the vicinity of the experimental reattachment locations. The simulations predict slightly longer recirculation regions for both the unforced and the controlled case. The results presented in this work suggest that, with the rapidly increasing computational resources of modern supercomputers such as the Cray X1, DNS is becoming a viable alternative to the use of turbulence models for investigating complex turbulent flows at moderately high Reynolds numbers.

Nomenclature

C_p	=	surface-pressure coefficient
c	=	chord length
$\boldsymbol{F}$	=	volume force
h	=	grid spacing
h_ξ, h_η	=	scale factors of the grid transformation
L	=	differential operator
$\mathcal{L}$	=	finite difference operator
l_k	=	Kolmogorov length scale
Re	=	Reynolds number
t_{ave}	=	averaging time
U_∞	=	freestream velocity
u, v, w	=	velocity components in the Cartesian (x, y, z) directions
$\boldsymbol{v}$	=	velocity vector
v_ξ, v_η	=	velocity components in the (ξ, η) directions
x, y, z	=	Cartesian coordinates
Δt	=	time step
ΔX, ΔY, ΔZ	=	extent of the computational domain
Δx^+, Δy^+, Δz^+	=	grid spacing in wall coordinates
δ^*	=	displacement thickness
θ	=	momentum thickness
ξ, η	=	generalized curvilinear coordinates
ψ	=	stream function
$\boldsymbol{\omega}$	=	vorticity vector
ω_ξ, ω_η, ω_z	=	vorticity components in the (ξ, η, z) directions
$\langle (\,)'(\,)' \rangle$	=	Reynolds-stress components

I. Introduction

THE accurate simulation of turbulent flows at high Reynolds numbers poses a formidable challenge in the field of computational fluid dynamics (CFD). Matters are especially complicated in the presence of turbulent flow separation, where accurate predictions of the complex flow dynamics are of critical importance if the unfavorable effects associated with the separation are to be reduced or avoided. Turbulent flow separation is often characterized by a superposition of small-scale turbulent motion and large coherent flow structures. Owing to their influence on the global flow behavior and, consequently, their importance for many technical applications, large coherent structures have been the focus of many investigations involving various prototypical flow geometries.[1,2] However, our understanding of turbulent flow separation, in general, is still far from complete. This lack of understanding can be attributed partly to the enormous computational resources required for high-resolution numerical simulations that would allow detailed insight into the relevant flow physics.

At present, most turbulent flows of engineering relevance are simulated by employing turbulence models that are implemented in CFD codes based on low-order discretization schemes. Although capable of providing adequate results in certain situations, to this date no turbulence models are universally applicable to a wide range of flows. In an effort to identify the state of the art in the computing of complex turbulent flows and to provide a reliable experimental database for the development and validation of new and improved models, a NASA Langley Research Center (LaRC) CFD Validation Workshop on Synthetic Jets and Turbulent Separation Control was held in Williamsburg, Virginia, in March 2004 (Ref. 3). For the third test case at this workshop, turbulent flow separation was considered, both with and without active flow control. The geometry that was chosen was a wall-mounted hump model, which was originally designed and investigated by Seifert and Pack.[4] A turbulent boundary layer passes over the upper surface of a Glauert–Goldschmied-type airfoil, and it separates as a result of the strong adverse pressure gradient encountered at the aft portion of the model. In their experiments, Seifert and Pack[4] found the global separation behavior to be relatively insensitive to upstream conditions as well as to the Reynolds number. The experiments for the CFD Validation Workshop were conducted by Greenblatt et al.[5,6] for a Reynolds number of slightly less than 10^5 (based on chord length). Detailed measurements of quantities such as static and dynamic surface pressure, wall shear stress, etc. Were obtained for the uncontrolled case as well as for cases with AFC by means of steady suction and periodic (zero efflux) excitation.

The excellent suitability of the wall-mounted hump geometry as a CFD validation test case resulted in the submission of 56 different cases by various researchers.[3] Whereas all the other workshop participants submitted results obtained from Reynolds-averaged Navier–Stokes (RANS) and/or hybrid RANS/large-eddy-Simulation (LES) calculations employing various turbulence models, the present investigation was aimed at assessing the feasibility

Received 26 October 2004; revision received 23 March 2005; accepted for publication 21 April 2005.

*Research Assistant, Department of Aerospace and Mechanical Engineering. Member AIAA.
†Professor, Department of Aerospace and Mechanical Engineering. Member AIAA.

of simulating complex turbulent flows by direct numerical simulations (DNS). For a comprehensive review of DNS as a research tool, the reader is referred to the article by Moin and Mahesh.[7] Some of the more recent efforts involving DNS of turbulent separation include those of Manhart and Friedrich[8] and Skote and Henningson.[9]

In the context of the present investigation, DNS refers to the direct solution of the Navier–Stokes equations without the use of turbulence models (either explicit or implicit), and not, as is typically done, to simulations in which all relevant time- and length scales are fully resolved. The present computations, however, should not be considered implicit large-eddy simulations (ILES) because the high-order numerical method presented in this paper was neither designed nor tested for the properties characteristic of ILES. Rather, the present investigation highlights the capabilities and limitations of current state-of-the-art Navier–Stokes solvers on modern supercomputers such as the Cray X1. In other words, in contrast to the work of Manhart and Friedrich,[8] for example, in which the Reynolds number was reduced compared to the experiments, the opposite approach is taken here: The turbulent flow is simulated at the (relatively high) experimental Reynolds number to allow for direct comparison with the experimental measurements and to shed light on the predictive capabilities of "coarse" DNS, that is, simulations that do not fully resolve the smallest scales of motion.

In the first part of the paper, the essential features of the numerical method that was used for the CFD Validation Workshop are discussed. Results are then presented and compared to experimental data for the unforced baseline case as well as for the controlled case by steady suction through a slot.

II. Numerical Method

A. Governing Equations

1. Vorticity-Velocity Formulation of the Navier–Stokes Equations

In the present work, the Navier–Stokes equations are solved in a vorticity-velocity formulation. This formulation is obtained by taking the curl of the momentum equation, thus eliminating the pressure term. Taking into consideration the fact that both velocity and vorticity vectors are solenoidal and using the following definition for the vorticity:

$$\boldsymbol{\omega} = -\nabla \times \boldsymbol{v} \tag{1}$$

the vorticity transport equation

$$\frac{\partial \boldsymbol{\omega}}{\partial t} + (\boldsymbol{v}\cdot\nabla)\boldsymbol{\omega} - (\boldsymbol{\omega}\cdot\nabla)\boldsymbol{v} = \frac{1}{Re}\nabla^2\boldsymbol{\omega} + \nabla\times\boldsymbol{F} \tag{2}$$

is obtained. The velocity field $\boldsymbol{v}$ is obtained from the vorticity $\boldsymbol{\omega}$ through the vector Poisson equation

$$\nabla^2\boldsymbol{v} = \nabla\times\boldsymbol{\omega} \tag{3}$$

The volume force $\boldsymbol{F}$ on the right-hand side of Eq. (2) will be discussed in Sec. III.

2. Governing Equations in General Orthogonal Coordinates

Let a general orthogonal coordinate system in two dimensions be denoted as (ξ, η, z), with

$$\boldsymbol{v} = v_\xi\cdot\boldsymbol{e}_\xi + v_\eta\cdot\boldsymbol{e}_\eta + w\cdot\boldsymbol{e}_z$$

$$\nabla = \boldsymbol{e}_\xi\cdot\frac{1}{h_\xi}\frac{\partial}{\partial\xi} + \boldsymbol{e}_\eta\cdot\frac{1}{h_\eta}\frac{\partial}{\partial\eta} + \boldsymbol{e}_z\cdot\frac{\partial}{\partial z} \tag{4}$$

Note that the spanwise direction was chosen to remain Cartesian to allow for pseudospectral treatment. Using the appropriate vector field functions,[10] the vorticity-velocity formulation of the Navier–Stokes equations in orthogonal curvilinear coordinates can be derived. The three components of the vorticity transport equation take the following form:

$$\begin{aligned}\frac{\partial\omega_\xi}{\partial t} + \frac{1}{h_\eta}\frac{\partial a}{\partial\eta} - \frac{\partial c}{\partial z} = \frac{1}{Re}\cdot\Bigg(&\frac{1}{h_\xi^2}\frac{\partial^2\omega_\xi}{\partial\xi^2} + \frac{1}{h_\eta^2}\frac{\partial^2\omega_\xi}{\partial\eta^2} + \frac{\partial^2\omega_\xi}{\partial z^2}\\ &+ cvta\cdot\frac{\partial\omega_\xi}{\partial\xi} + cvtb\cdot\frac{\partial\omega_\xi}{\partial\eta} + cvtc\cdot\omega_\xi + cvtd\cdot\frac{\partial\omega_\eta}{\partial\xi}\\ &+ cvte\cdot\frac{\partial\omega_\eta}{\partial\eta} + cvtf\cdot\omega_\eta\Bigg) + (\nabla\times\boldsymbol{F})_\xi\end{aligned} \tag{5a}$$

$$\begin{aligned}\frac{\partial\omega_\eta}{\partial t} - \frac{1}{h_\xi}\frac{\partial a}{\partial\xi} + \frac{\partial b}{\partial z} = \frac{1}{Re}\cdot\Bigg(&\frac{1}{h_\xi^2}\frac{\partial^2\omega_\eta}{\partial\xi^2} + \frac{1}{h_\eta^2}\frac{\partial^2\omega_\eta}{\partial\eta^2} + \frac{\partial^2\omega_\eta}{\partial z^2}\\ &+ cvta\cdot\frac{\partial\omega_\eta}{\partial\xi} + cvtb\cdot\frac{\partial\omega_\eta}{\partial\eta} + cvtc\cdot\omega_\eta - cvtd\cdot\frac{\partial\omega_\xi}{\partial\xi}\\ &- cvte\cdot\frac{\partial\omega_\xi}{\partial\eta} - cvtf\cdot\omega_\xi\Bigg) + (\nabla\times\boldsymbol{F})_\eta\end{aligned} \tag{5b}$$

$$\begin{aligned}\frac{\partial\omega_z}{\partial t} + \frac{1}{h_\xi}\frac{\partial c}{\partial\xi} - \frac{1}{h_\eta}\frac{\partial b}{\partial\eta} - \frac{1}{h_\xi h_\eta}\left(\frac{\partial h_\xi}{\partial\eta}\cdot b - \frac{\partial h_\eta}{\partial\xi}\cdot c\right)&\\ = \frac{1}{Re}\cdot\Bigg(\frac{1}{h_\xi^2}\frac{\partial^2\omega_z}{\partial\xi^2} + \frac{1}{h_\eta^2}\frac{\partial^2\omega_z}{\partial\eta^2} + \frac{\partial^2\omega_z}{\partial z^2}&\\ + cvta\cdot\frac{\partial\omega_z}{\partial\xi} + cvtb\cdot\frac{\partial\omega_z}{\partial\eta}\Bigg) + (\nabla\times\boldsymbol{F})_z&\end{aligned} \tag{5c}$$

In the preceding equations, a, b, and c are the nonlinear terms

$$a = v_\eta\omega_\xi - v_\xi\omega_\eta, \qquad b = w\omega_\eta - v_\eta\omega_z, \qquad c = v_\xi\omega_z - w\omega_\xi \tag{6}$$

The Poisson equations for the velocities, obtained from Eq. (3), are

$$\begin{aligned}\frac{\partial^2 v_\xi}{\partial\xi^2} + cpla_\xi\cdot\frac{\partial^2 v_\xi}{\partial z^2} + cplb_\xi\cdot\frac{\partial v_\xi}{\partial\xi} + cplc_\xi\cdot v_\xi&\\ = cpra_\xi\cdot\frac{\partial\omega_\eta}{\partial z} + cprb_\xi\cdot v_\eta + cprc_\xi\cdot\frac{\partial v_\eta}{\partial\xi}&\\ + cprd_\xi\cdot\frac{\partial v_\eta}{\partial\eta} + cpre_\xi\cdot\frac{\partial^2 v_\eta}{\partial\xi\,\partial\eta}&\end{aligned} \tag{7a}$$

$$\begin{aligned}\frac{\partial^2 v_\eta}{\partial\xi^2} + cpla_\eta\cdot\frac{\partial^2 v_\eta}{\partial\eta^2} + cplb_\eta\cdot\frac{\partial^2 v_\xi}{\partial z^2}&\\ + cplc_\eta\cdot\frac{\partial v_\eta}{\partial\xi} + cpld_\eta\cdot\frac{\partial v_\eta}{\partial\eta} + cple_\eta\cdot v_\eta&\\ = cpra_\eta\cdot\frac{\partial\omega_\xi}{\partial z} + cprb_\eta\cdot\frac{\partial\omega_z}{\partial\xi}&\\ + cprc_\eta\cdot\omega_z + cprd_\eta\cdot v_\xi + cpre_\eta\frac{\partial v_\xi}{\partial\xi}&\end{aligned} \tag{7b}$$

$$\begin{aligned}\frac{\partial^2 w}{\partial\xi^2} + cpla_z\cdot\frac{\partial^2 w}{\partial z^2} + cplb_z\cdot\frac{\partial w}{\partial\xi}&\\ = cpra_z\cdot\frac{\partial\omega_\eta}{\partial\xi} + cprb_z\cdot\omega_\eta + cprc_z\cdot\frac{\partial v_\eta}{\partial z} + cprd_z\cdot\frac{\partial^2 v_\eta}{\partial\eta\partial z}&\end{aligned} \tag{7c}$$

The coefficients that appear in Eqs. (5) and (7) are listed in the Appendix.

The flow is assumed to be periodic in the spanwise z direction. As a result, the flow variables are expanded in Fourier cosine and sine series. Each variable is represented by a total of $2K+1$ Fourier modes: the $2D$ spanwise average (zeroth Fourier mode) and K symmetric Fourier cosine as well as K antisymmetric Fourier sine modes. As a result of this decomposition, the three-dimensional governing equations reduce to a set of two-dimensional equations for each Fourier mode.

The set of boundary conditions for the governing equations is discussed in Sec. III.B, except for the wall-vorticity computation, which is described in Sec. II.B.

B. Numerical Procedure for Solving the Governing Equations

The present curvilinear Navier–Stokes solver was adapted from a highly optimized Cartesian code developed by Meitz and Fasel.[11] In spite of the increased complexity of the curvilinear governing equations, many elements and features of the original code could be maintained.

1. Integration of the Vorticity Transport Equations

Standard $\mathcal{O}(h^4)$ accurate compact differences[12] are employed for the discretization of the derivatives on the right-hand sides of Eqs. (5). The only exception are the ξ derivatives of the nonlinear terms, which are treated using $\mathcal{O}(h^4)$ accurate split compact differences.[11] These split differences provide superior short-wave resolution characteristics at no additional computational cost. The time integration of the governing equations is performed using an explicit, four-stage, $\mathcal{O}[(\Delta t)^4]$ accurate Runge–Kutta scheme.[13]

2. Multigrid Solution of the Wall-Normal Velocity Equation

As a result of the transformation to curvilinear coordinates (and after expanding the variables in Fourier series), Eq. (7b) changes from a regular Poisson-type equation to a two-dimensional convection-diffusion equation with variable coefficients. This equation is of the form

$$\frac{\partial^2\phi}{\partial\xi^2} + \alpha(\xi,\eta)\cdot\frac{\partial^2\phi}{\partial\eta^2} + \beta(\xi,\eta)\cdot\frac{\partial\phi}{\partial\xi} + \gamma(\xi,\eta)\cdot\frac{\partial\phi}{\partial\eta} + \delta(\xi,\eta)\cdot\phi = \rho(\xi,\eta) \tag{8}$$

and its solution represents the single most computationally expensive step in the numerical integration of the governing equations. Because the derivation of $\mathcal{O}(h^4)$ accurate compact difference stencils for Eq. (8) is greatly complicated by the presence of the first-derivative terms and the variable coefficients, the procedure of Dennis and Hudson[14] is employed and generalized to take into account the presence of the coefficient $\alpha(\xi,\eta)$. Equation (8) at grid point (i, j) is split into two equations:

$$(\phi_{\xi\xi})_{i,j} + \beta_{i,j}\cdot(\phi_\xi)_{i,j} = r_{i,j} \tag{9a}$$

$$\rho_{i,j} - \alpha_{i,j}\cdot(\phi_{\eta\eta})_{i,j} - \gamma_{i,j}\cdot(\phi_\eta)_{i,j} - \delta_{i,j}\cdot\phi_{i,j} = r_{i,j} \tag{9b}$$

The two equations are (temporarily) treated as separate ordinary differential equations (ODEs) and auxiliary functions are introduced to eliminate the first-derivative terms. Equation (9a) is treated in the same way as proposed by Dennis and Hudson.[14] For Eq. (9b), however, a slightly more complicated auxiliary function is required to eliminate the inconvenient first-derivative term,

$$\zeta = \exp\left\{\int_{\eta_0}^{\eta}\frac{1}{\alpha(y)}\left[\frac{\gamma(y)}{2} - \frac{\partial\alpha}{\partial y}\right]\mathrm{d}y\right\}\cdot\alpha\cdot\phi \tag{10}$$

The function ζ satisfies the equation

$$\zeta'' - \frac{1}{4\alpha^2}[\gamma^2 - 2\gamma\alpha' + 2\alpha(-2\delta+\gamma')]\cdot\zeta = \exp\left\{\int_{\eta_0}^{\eta}\frac{1}{\alpha(y)}\left[\frac{\gamma(y)}{2} - \frac{\partial\alpha}{\partial y}\right]\mathrm{d}y\right\}\cdot(\rho - r) \tag{11}$$

which can now be discretized using standard $\mathcal{O}(h^4)$ accurate compact differences. The final step of adding the two separate finite difference approximations to produce a single, nine-point difference stencil once again follows the procedure of Dennis and Hudson, that is, the remaining derivative terms can be discretized using $\mathcal{O}(h^2)$-accurate central differences without jeopardizing the overall $\mathcal{O}(h^4)$ accuracy of the approximation.[14]

The linear system of equations that results from the discretization just described is solved using a zebra alternating line Gauss–Seidel (see Ref. 15) (ZALGS) iteration with multigrid acceleration. The slightly inferior smoothing properties of the ZALGS algorithm compared to other iteration schemes (e.g., incomplete line LU decomposition[1]) are compensated for by the fact that the ZALGS can easily be vectorized and/or parallelized. This is especially important on vector-parallel supercomputers such as the Cray X1.

The multigrid is implemented using a standard V-Cycle technique[16] in combination with full weighting as restriction operator and interpolation as prolongation operator. For the purpose of validating the accuracy of the discretization and the proper implementation of the multigrid algorithm, consider the Poisson equation

$$\frac{\partial^2\phi}{\partial x^2} + \frac{\partial^2\phi}{\partial y^2} = \rho(x,y), \qquad \phi(x,y) = \sin(3\pi x)^2 e^{-4x^2}\sin(2\pi y)^2 \tag{12}$$

in a domain $0 \le x \le 1, 0 \le y \le 1$, subject to $\phi = 0$ everywhere on the boundary. Equation (12) is solved on both equidistant and stretched grids ranging in size from 65×65 points to 513×513 points. The l_∞ and l_2 norms of the discretization errors are plotted vs grid size in Fig. 1. The theoretical $\mathcal{O}(h^4)$ convergence behavior is included for reference. As expected, both l_∞ and l_2 norms decay by a factor of 16 when the grid spacing is halved. Even on stretched grids, where "convective terms" are introduced during the transformation of Eq. (12), the high-order convergence behavior remains intact.

3. Solution of the Streamwise/Spanwise Velocity Equations

When expressing the flow variables in terms of Fourier series, both Eq. (7a) and Eq. (7c) are of the form

$$\frac{\partial^2\phi}{\partial\xi^2} + \alpha(\xi,\eta)\cdot\frac{\partial\phi}{\partial\xi} + \beta(\xi,\eta)\cdot\phi = \rho(\xi,\eta) \tag{13}$$

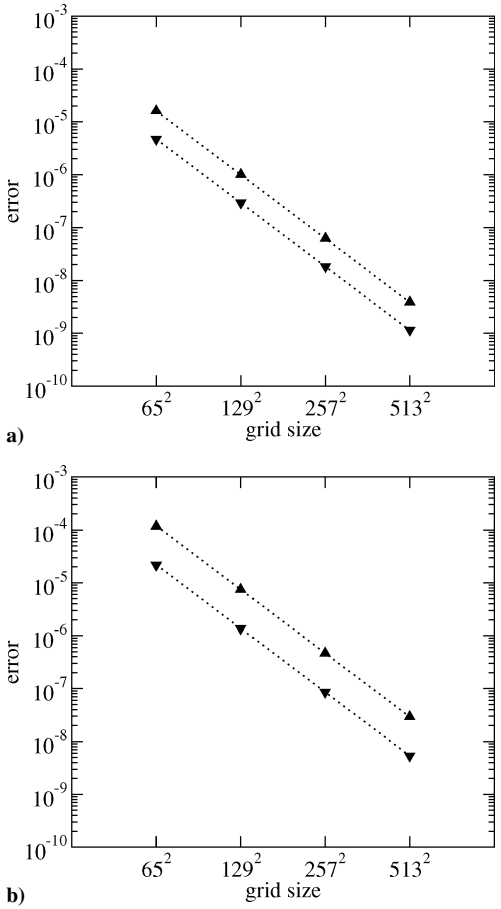

Fig. 1 Multigrid validation: convergence behavior of the nine-point finite difference stencil: ▲, l_∞ norm; ▼, l_2 norm; and · · · ·, theoretical $\mathcal{O}(h^4)$ convergence.

The derivation of a $\mathcal{O}(h^4)$-accurate compact stencil is as follows: Rewrite Eq. (13) at grid point (i, j) as

$$(\mathcal{L}\phi)_{i,j} = (\phi_{\xi\xi})_{i,j} + \alpha_{i,j} \cdot (\phi_\xi)_{i,j} + \beta_{i,j} \cdot \phi_{i,j} = \rho_{i,j} \tag{14}$$

Now, the following relation between $(\mathcal{L}\phi)$ and ϕ is sought:

$$(\mathcal{L}\phi)_{i,j} + C_1 \cdot (\mathcal{L}\phi)_{i-1,j} + C_2 \cdot (\mathcal{L}\phi)_{i+1,j} = C_3 \cdot \phi_{i-1,j} + C_4 \cdot \phi_{i,j} + C_5 \cdot \phi_{i+1,j} \tag{15}$$

After substituting $(\mathcal{L}\phi)_{i,j} = (\phi_{\xi\xi})_{i,j} + \alpha_{i,j} \cdot (\phi_\xi)_{i,j} + \beta_{i,j} \cdot \phi_{i,j}$, etc. into Eq. (15), the terms $(\phi_\xi)_{i-1,j}$, $(\phi_\xi)_{i+1,j}$, $(\phi_{\xi\xi})_{i-1,j}$, and $(\phi_{\xi\xi})_{i+1,j}$ are expanded in Taylor series about (i, j). The coefficients C_1 to C_5 can then be determined such that all terms up to (and including) $\mathcal{O}(h^4)$ are eliminated. Once the coefficients are computed, the right-hand side of Eq. (14) can be substituted into Eq. (15). The resulting tridiagonal system of equations (for each grid line $j = \text{const}$) can be solved very efficiently using the Thomas algorithm,[13] while taking full advantage of the vector-parallel architecture of the Cray X1.

4. Calculation of the Wall-Vorticity

One of the difficulties associated with the numerical solution of the incompressible Navier–Stokes equations in the vorticity-velocity formulation is the lack of "proper" boundary conditions for the streamwise ω_ξ and spanwise ω_z vorticity components at the wall. The same procedure as used in other incompressible Navier–Stokes solvers based on the vorticity-velocity formulation is adopted here: the numerical method is designed such that the wall-vorticity values are not required for the solution of the velocity field at the new time level. This new velocity field is then used to update the vorticity components at the wall, such as to ensure consistency and zero divergence of the velocity and vorticity fields[11,17]:

$$\frac{\partial^2\omega_\xi}{\partial\xi^2} + cwla_\xi \cdot \frac{\partial^2\omega_\xi}{\partial z^2} + cwlb_\xi \cdot \frac{\partial\omega_\xi}{\partial\xi} = cwra_\xi \cdot \frac{\partial}{\partial\eta}[h_\xi \cdot \omega_\eta] + cwrb_\xi \cdot \frac{\partial^2}{\partial\eta\partial\xi}[h_\xi \cdot \omega_\eta] + \frac{\partial}{\partial z}[L(v_\eta) - L(v_\xi)] \tag{16a}$$

$$cprb_\eta \cdot \frac{\partial\omega_z}{\partial\xi} + cprc_\eta \cdot \omega_z = -cpra_\eta \cdot \frac{\partial\omega_\xi}{\partial z} + L(v_\eta) - L(v_\xi) \tag{16b}$$

In Eqs. (16), $L(v_\eta)$ and $L(v_\xi)$ are the differential operators associated with v_η and v_ξ in Eq. (7b). Equation (16a) is obtained by taking the ξ derivative of $\nabla \cdot \boldsymbol{\omega} = 0$ and by eliminating the the ω_z term via the z derivative of Eq. (7b). Equation (16b) is identical to Eq. (7b), with the exception that ω_z now represents the dependent variable.

5. Parallelization on the Cray X1

One of the challenges associated with efficient parallel implementations of high-order methods for the incompressible Navier–Stokes equations is the fact that the global nature of the governing equations complicates the use of typical domain decomposition techniques. The classical approach of arbitrarily subdividing the computational domain (as is typically done in compressible Navier–Stokes codes) requires additional iteration loops that often negate the benefits achieved by the parallelization. However, domain decomposition techniques that preserve the global nature of the governing equations require extensive amounts of interprocessor communication. In the past, before the introduction of the newest generation of supercomputers like the Cray X1, the requirement for low-latency, high-bandwidth processor interconnect prevented the implementation of efficient parallel domain decomposition techniques into state-of-the-art incompressible Navier–Stokes codes.

The parallelization of the code is performed by using the message-passing interface. The domain is decomposed with respect to the Fourier modes, therefore preserving the linear systems that need to be solved as a result of the compact differences as well as the Poisson equations. Each time the flowfield is transformed from spectral to physical space and back, the entire three-dimensional arrays are transposed and redistributed among the processors. Despite the communication overhead involved in this task, the efficiency of this algorithm on the Cray X1 is very high. Parallel performance results for typical simulations are shown in Fig. 2. These three-dimensional benchmark calculations were performed on the 256 CPU Cray X1 at the Army High Performance Computing Research Center. [In the present paper, CPU refers to the so-called multistreaming processor on the Cray X1. Each MSP, which consists of four single-streaming processors, is rated at a theoretical peak performance of 12.8 Gflop/s.] The problem size was increased along with the number of CPUs and ranged from ~2.1 million points ($513 \times 513 \times 8$) on 1 CPU to ~135 million points ($513 \times 513 \times 512$) on 64 CPUs. The speed-up is shown in Fig. 2a; the parallel efficiency is shown in Fig. 2b. The code scales very well, especially when considering the amount of data communication that is required for such large simulations. For 64 CPUs, the speed-up is 43, which corresponds to a parallel efficiency of approximately 67%.

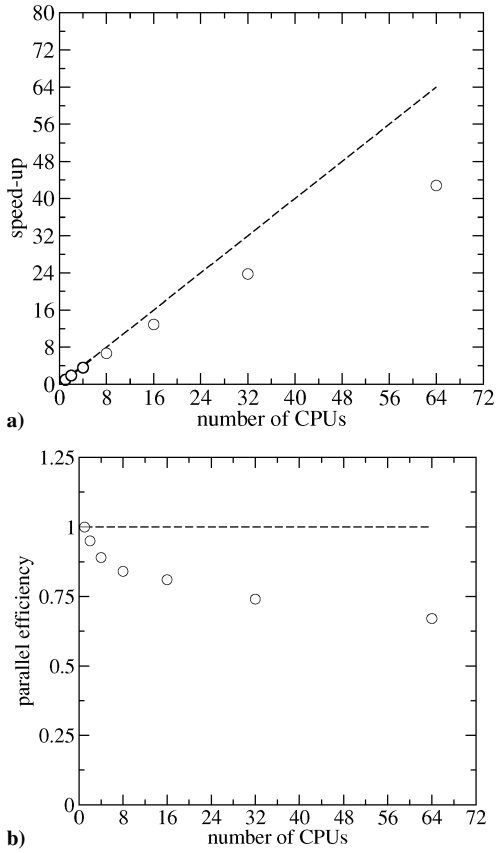

Fig. 2 Parallel performance on the Cray X1: a) speed-up; b) parallel-efficiency; - - - -, ideal performance and ○, actual performance.

III. Simulation Setup

As mentioned in the Introduction, the geometry considered in the present investigation simulates the upper surface of a modified Glauert–Goldschmied-type airfoil,[4] as investigated experimentally[5,6] at NASA LaRC for the CFD Validation of Synthetic Jets and Turbulent Separation Control Workshop.

A. Grid and Computational Parameters

The grid used for the simulations is shown in Fig. 3. It was obtained from an iterative solver that was developed to generate orthogonal curvilinear grids based on the method of Duraiswami and Prosperetti.[18] At each step of the iteration, the set of equations

$$\frac{\partial}{\partial\xi}\left(g\frac{\partial x_i}{\partial\xi}\right) + \frac{\partial}{\partial\eta}\left(\frac{1}{g}\frac{\partial x_i}{\partial\eta}\right) = 0, \qquad i = 1, 2 \tag{17}$$

is solved using a multigrid algorithm similar to the one used in the Navier–Stokes code. The distribution of boundary points is obtained from a Newton–Raphson subiteration. Control over grid point clustering is provided by appropriate specification of the distortion function g. The grid generator was vectorized and ported to the Cray X1 because in order to obtain a high-quality orthogonal grid, Eqs. (17) need to be solved hundreds of thousands of times.

The grid consists of 2049 points in the streamwise direction and 321 points in the wall-normal direction. The number of collocation points (for the computation of the non-linear terms in physical space) is 320, which results in a total number of approximately 210 million grid points. As such, the present grid is approximately 100 times larger than that of any other submission for case 3 of the CFD Validation Workshop.[3]

The simulations were performed on 32 Cray X1 CPUs at the AHPCRC. The turnaround time for simulating one characteristic "flow-over time" (i.e., the time it takes for a fluid particle in the free stream to travel one chord length) for the baseline case is approximately 10 h. The relevant computational parameters are summarized in Table 1.

B. Boundary Conditions

An illustration of the computational domain for the Navier–Stokes simulations is given in Fig. 4. At the inflow boundary $x/c = -1.05$, a laminar Blasius boundary-layer profile is imposed with $Re_x = 22.6 \times 10^6$. All velocity and vorticity components are prescribed as Dirichlet conditions. For maintaining the fourth-order accuracy of the code, the streamwise derivatives are prescribed as well. To prevent reflections from the outflow boundary, turbulent fluctuations are damped out in a buffer domain starting at $x/c = 1.7$

Table 1 Relevant computational parameters

Parameter	Value
Domain size ($\Delta X/c$, $\Delta Y/c$, $\Delta Z/c$)	3.25, 0.9, 0.142
Number of grid points in x, y	2049, 321
Number Fourier modes in z $(2K+1)$	193
Number of collocation points in z	320
Total number of points	$\approx 210 \times 10^6$
Δx^+, Δy^+, Δz^+ (based on $x/c = -0.5$)	27–92, 1.2, 17
Δt (baseline case)	3.3×10^{-4}
Δt (suction case)	1.4×10^{-4}
t_{ave} (mean flow quantities)	≈ 6
t_{ave} (Reynolds stresses)	≈ 8

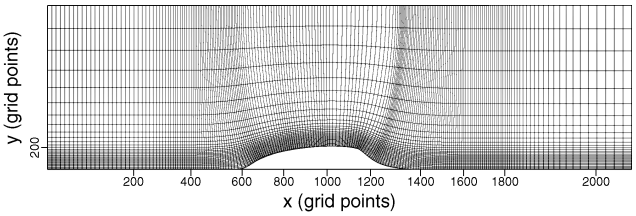

Fig. 3 Computational grid; every 10th point shown in both x and y.

using the approach proposed by Meitz and Fasel.[11] At the upper boundary, a slip wall is imposed, $v = 0$, and irrotational flow is assumed, $\boldsymbol{\omega} = 0$. Because the equations for the streamwise v_ξ and spanwise w velocity components reduce to ODEs in the streamwise direction, no upper boundary conditions are required for these quantities. At the wall, no-slip and no-penetration conditions are imposed, except over the suction slot at $x/c \approx 0.65$. Periodicity is assumed in the spanwise direction with the domain width chosen as $\Delta Z/c = 0.142$. This domain width was chosen as a compromise to achieve a reasonable spanwise resolution. The choice was also based on the assumption that the coherent structures present in this flow are predominantly two dimensional in nature.

For the case involving steady suction, the slot is modeled by a boundary condition on the wall-normal velocity component,

$$v_{\text{suct}} = A_{\text{suct}} \cdot \{\cos[2\pi(s/w_{\text{slot}})]\}^3 \tag{18}$$

where s represents the distance from the center of the slot along the body surface. The width of the slot w_{slot} was increased to obtain a reasonable spatial resolution (Fig. 4). The strength of the suction $A_{\text{suct}} = -0.3$ was adjusted accordingly to match the specified suction rate of 0.015 kg/s.

C. Tripping of the Laminar Boundary Layer

The laminar boundary layer is tripped to turbulence near the inflow boundary (Fig. 4) by introducing high-amplitude, three-dimensional disturbances into the flow using a volume forcing technique,[19] that is, by adding a time-harmonic forcing term $\nabla \times \boldsymbol{F}$ to the right-hand side of the vorticity transport equations (2). The force is applied for selected spanwise Fourier components k. For each of these k, it takes on the form of

$$\boldsymbol{F}^{(k)}(\xi, \eta, k, t) = \sum_{n=1}^{N} \boldsymbol{A}_{\text{vf}}^{(n,k)} \cos\left[2\pi f^{(n,k)} t + \theta_{\text{vf}}^{(n,k)}\right] S_{\text{vf}}^{(n,k)}(\xi, \eta) \tag{19}$$

where vector $\boldsymbol{A}_{\text{vf}}^{(n,k)}$ determines the amplitude and spatial orientation of the force and $f^{(n,k)}$ and $\theta_{\text{vf}}^{(n,k)}$ are the frequency and phase angle in time. The spatial distribution of the volume force $S_{\text{vf}}^{(n,k)}$ has the Gaussian shape

$$S_{\text{vf}}^{(n,k)} = \exp\left\{-\left[\frac{\xi - \xi_{\text{vf}}^{(n,k)}}{a_{\text{vf}}^{(n,k)}}\right]^2 - \left[\frac{\eta - \eta_{\text{vf}}^{(n,k)}}{b_{\text{vf}}^{(n,k)}}\right]^2\right\} \tag{20}$$

with $a_{\text{vf}}^{(n,k)}$ and $b_{\text{vf}}^{(n,k)}$ determining its size. The wall-normal forcing locations were chosen such as to achieve maximum receptivity of the flow to the disturbance input. Because of the forcing, the flow rapidly transitions to turbulence, and the boundary-layer profiles approach the characteristic log-law behavior upstream of the hump model (see Fig. 5). As a result of the tripping procedure just described, it was found to be difficult to precisely match a particular turbulent profile at a given streamwise location. Because of the limitations on available computational resources, it was impossible to trip a laminar boundary layer, match the given turbulent profile at $x/c = -2.14$, and continue the computation all of the way to and beyond the hump.

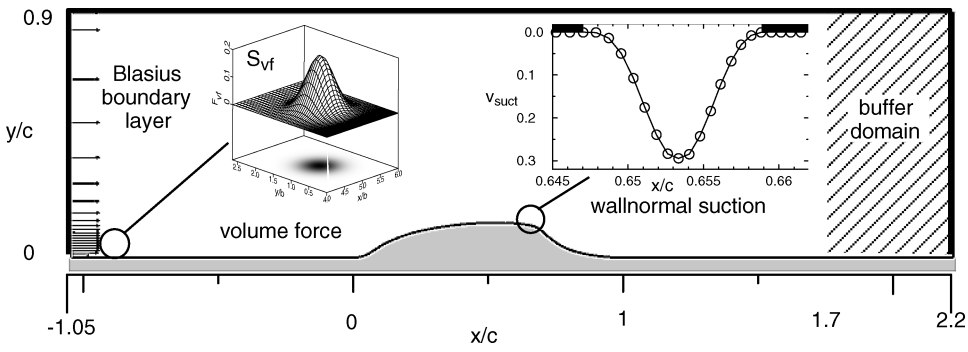

Fig. 4 Sketch of the computational domain.

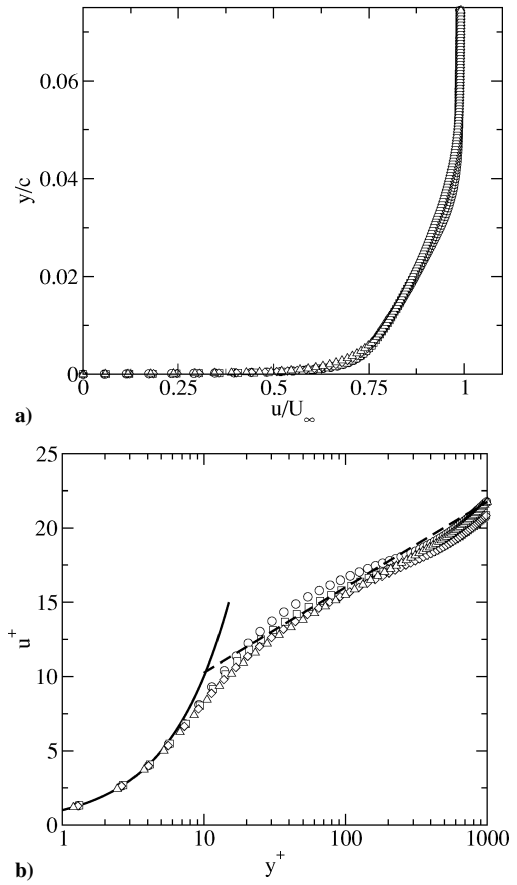

Fig. 5 Streamwise velocity profiles upstream of the hump: ○, $x/c = -0.5$; □, $x/c = -0.4$; ◇, $x/c = -0.3$; and △ $x/c = -0.2$.

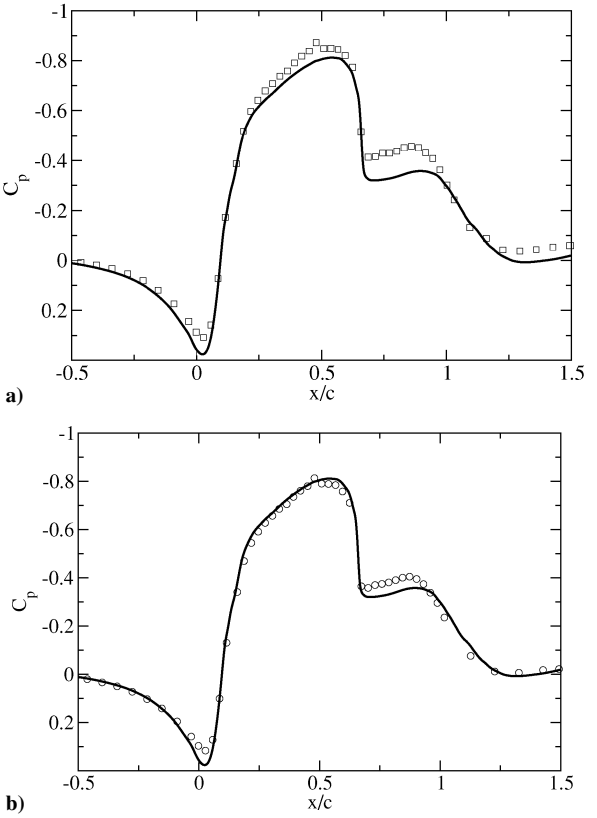

Fig. 6 Surface-pressure coefficient for the baseline case: a) □, experimental data with endplates and ——, simulation; and b) ○, experimental data without endplates and ——, simulation.

Because it was noted by Seifert and Pack[4] that, in their experiments, the thickness of the upstream boundary layer had only a minor effect on the flowfield, it was deemed more important to reach a turbulent state upstream of the hump than to precisely match the experimental boundary layer. In the present simulations, the approach boundary layer is thinner than the one in the experiments.[6] At the streamwise location $x/c = -0.5$, for example, the Reynolds numbers based on displacement and momentum thickness are $Re_{\delta^*} \approx 5.2 \times 10^3$ and $Re_\theta \approx 4 \times 10^3$, respectively.

IV. Results

A. Baseline Case

The surface-pressure coefficient C_p from the DNS of the baseline case is presented in Fig. 6 and compared to experimental data.[6] The data points in the plot on Fig. 6a represent the original measurements where endplates were mounted at either side of the hump model. The numerical result reveals a notable underprediction of the suction peak on top of the hump. Because this underprediction was also present in almost all of the simulations by other investigators presented at the CFD Validation Workshop,[3] blockage effects caused by the side-mounted endplates in the experiments were suggested as one possible cause for this systematic discrepancy. The C_p measurements for the baseline case were subsequently repeated with the endplates (temporarily) removed. The comparison of the present numerical C_p prediction with these "new" measurements is shown in the plot in Fig. 6b. The agreement between experiment and simulation is much improved, and the suction peak is now correctly predicted by the DNS. Differences in the C_p distributions are still apparent for the region downstream of the separation location. The pressure plateau between $x/c \approx 0.67$ and 0.88, which corresponds to the "dead-air" region in the separation bubble, remains slightly too high (even though a significant improvement is apparent in comparison to the original measurements). This mismatch was also observed by most of the other participants of the CFD Validation Workshop, but the cause for this discrepancy remains unknown.

Depsite the good agreement of the pressure distributions, the simulations predict a slightly longer recirculation length. The mean reattachment point in the experiments was measured at $x/c \approx 1.11$, while the DNS predicts a value of $x/c \approx 1.19$ (based on the spanwise wall vorticity). This corresponds to an overprediction of the reattachment length of approximately 20%. However, the experimental reattachment location (as well as all other experimental data presented in the remainder of this paper) was obtained from measurements in which the side-mounted endplates were included.

Time and spanwise averaged streamlines and velocity profiles downstream of the separation point are presented in Fig. 7. The streamlines clearly illustrate the recirculation region as well as the reattachment point at $x/c \approx 1.19$. The streamwise u and vertical v velocity profiles are shown alongside experimental data points (the v-velocity profiles are magnified by a factor of 5 relative to the u profiles). The velocity profiles are in excellent agreement with the experiments at the locations $x/c = 0.7$, 0.8, and 0.9. This observation corroborates the finding that the thickness of the approach boundary layer (upstream of the hump) has only a minor effect on the flow characteristics.[4] The small discrepancies that are apparent downstream of $x/c = 1$ are likely related to the shorter recirculation region in the experiments. Although the reason for the overprediction of the reattachment length in the simulations is unknown, it seems appropriate to point out two potential causes.

First, it is apparent that the present "coarse" DNS is not resolved all of the way down to the smallest scales. Assuming that the Kolmogorov length scale behaves as $l_k = \mathcal{O}(Re^{-3/4})$, the physical resolution of the present simulation can be estimated as $\Delta x = \mathcal{O}(10 \cdot l_k)$, $\Delta y|_{\text{wall}} = \mathcal{O}(l_k)$, and $\Delta z = \mathcal{O}(10 \cdot l_k)$. In other words, there is a possibility that further refinement of the grid could result in an improved prediction of the reattachment length. A grid-resolution study, however, was beyond the scope of this

investigation (because of limitations on available computational resources).

Second, a higher freestream turbulence level might have been present in the experiments, especially in the range of frequencies to which the separated shear layer is hydrodynamically unstable. (Unfortunately, freestream turbulence measurements were not available from the experiments for this particular configuration.) In other words, if the two-dimensional component of the disturbances at the "proper" frequencies were higher in the experiments than in the DNS, large, spanwise coherent structures would form farther upstream than in the simulations. These structures, in turn, promote the entrainment of high-momentum fluid that is required for reattaching the flow. The formation of such coherent structures is illustrated in Figs. 8 and 9. Shown are instantaneous gray-scale contours of the spanwise vorticity component in a side view (Fig. 8) and in a top view toward the surface (Fig. 9). The separated shear layer is clearly visible in the side view, and it can be seen to roll up and form what can be identified as a large clockwise-rotating structure in the region between $x/c = 1$ and 1.1. The spanwise coherence of this structure is illustrated in Fig. 9, where the bright area represents the "footprint" of the structure.

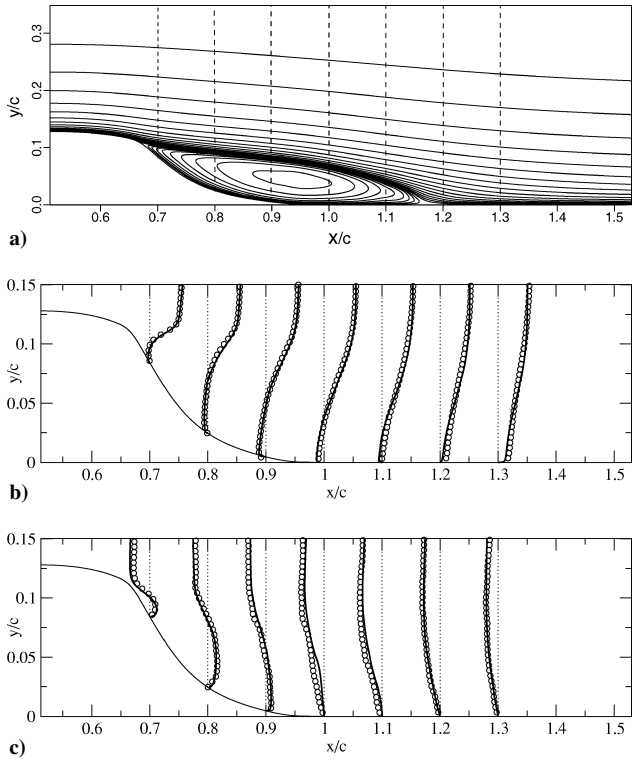

Fig. 7 Time- and spanwise-averaged simulation results in comparison to experimental data for the baseline case: ○, experimental data and ——, simulation results; a) streamlines (equidistant contours of $\ell_n|5 \times 10^3 \times \psi| + 1$), b) streamwise velocity profiles, and c) vertical velocity profiles (magnified by a factor of 5 relative to the streamwise velocity profiles).

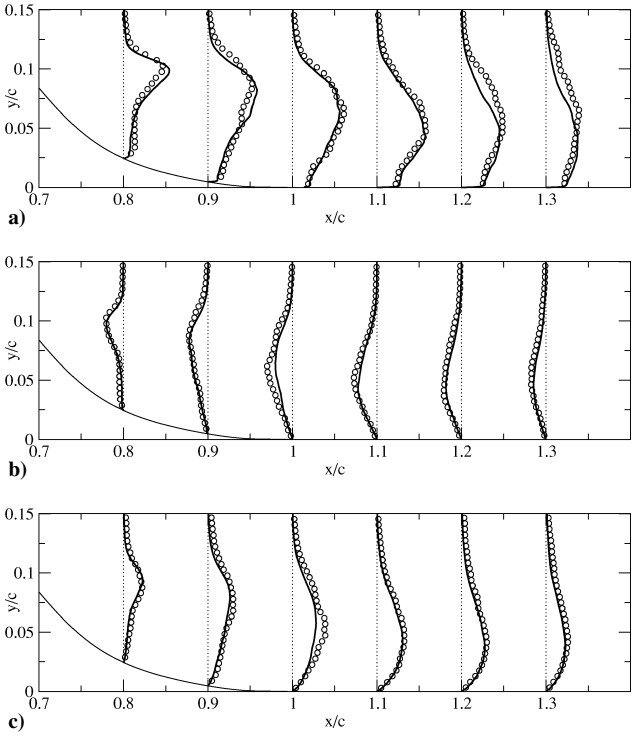

Fig. 10 Time- and spanwise-averaged simulation results in comparison to experimental data for the baseline case: ○, experimental data and ——, simulation results; a) $\langle u'u' \rangle$, b) $\langle u'v' \rangle$, and c) $\langle v'v' \rangle$.

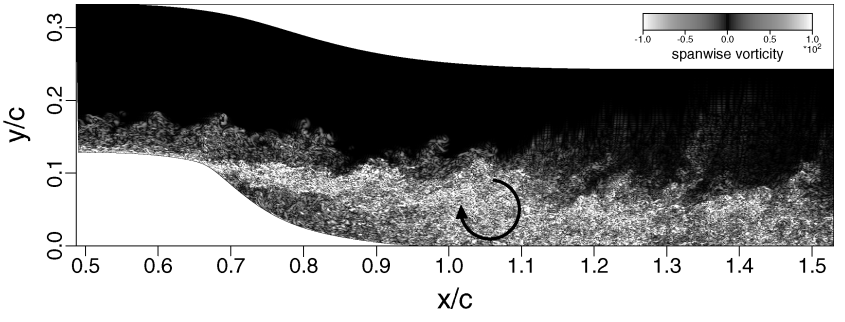

Fig. 8 Instantaneous gray-scale contours of the spanwise vorticity component (side view). Baseline case.

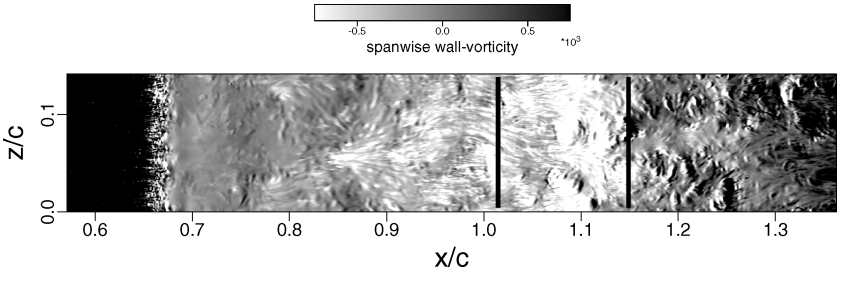

Fig. 9 Instantaneous gray-scale contours of the spanwise wall-vorticity component (top view). Baseline case.

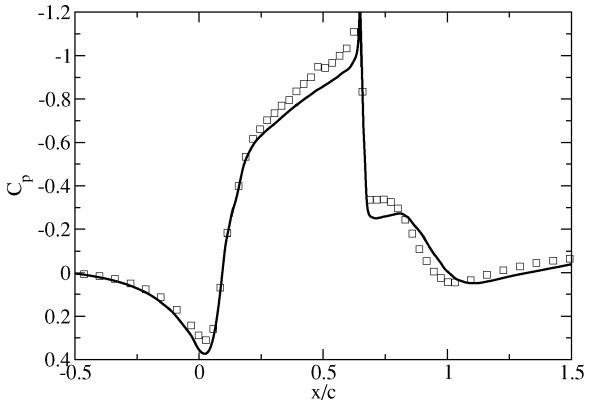

Fig. 11 Surface-pressure coefficient for the suction case: □, experimental data (with endplates) and ——, simulation.

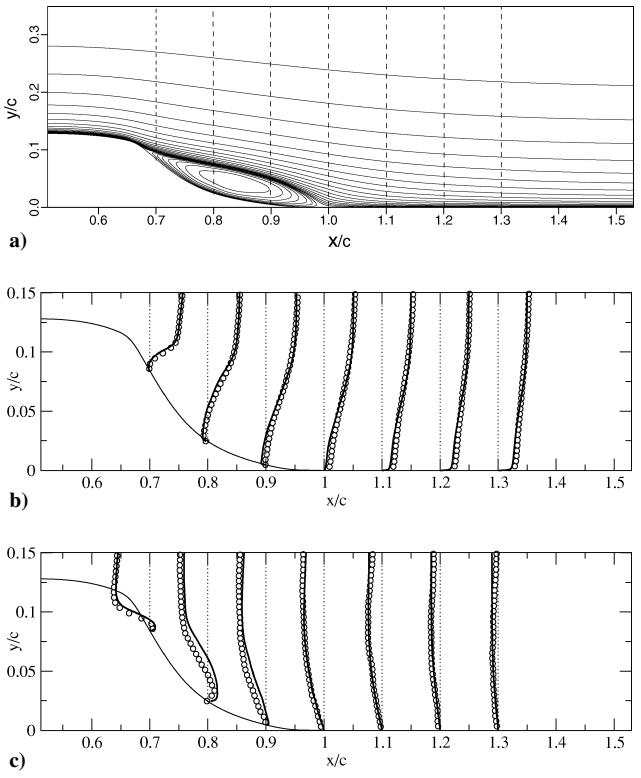

Fig. 12 Time- and spanwise-averaged simulation results in comparison to experimental data for the suction case: ○, experimental data and ——, simulation results; a) streamlines (equidistant contours of $\ell_n[5 \times 10^3 \times \psi] + 1$), b) streamwise velocity profiles, and c) vertical velocity profiles (magnified by a factor of 5 relative to the streamwise velocity profiles).

A more definitive statement about the extent to which coherent structures might be responsible for the overprediction of the reattachment length in the numerical simulations can be made only once detailed frequency spectra are available from the experiments for comparison.

A detailed comparison of selected Reynolds-stress components at various streamwise locations downstream of the separation point is given in Fig. 10. Shown are distributions of $\langle u'u' \rangle$ (Fig. 10a), $\langle u'v' \rangle$ (Fig. 10b), and $\langle v'v' \rangle$ (Fig. 10c). Overall, the agreement between the experimental measurements and the numerical predictions is very good. This observation is particularly important in that it shows that even for coarse DNS the predictive capabilities can extend beyond the basic mean flow quantities.

B. Steady Suction

The surface-pressure coefficient C_p for the DNS of the steady suction case is presented in Fig. 11 in comparison with the experiments. The experimental data points were obtained from measurements in which the endplates caused blockage. Assuming that, if the endplates were removed, the same trend would hold as for the baseline case, the agreement between simulation and experiments is excellent everywhere except in the region downstream of $x/c \approx 0.85$. Once again, the DNS overpredicts the reattachment length slightly. The reattachment point in the experiments is located at $x/c \approx 0.94$ vs $x/c \approx 1.0$ in the DNS.

Time- and spanwise-averaged streamlines and velocity profiles downstream of the separation point are presented in Fig. 12. Comparison of the streamlines with those of the baseline case (Fig. 7) reveals a much shorter and shallower separation bubble for the case with suction. The velocity profiles are in good agreement with the experimental measurements at $x/c = 0.7$, but notable differences are already visible at $x/c = 0.8$. The reason that discrepancies set in farther upstream compared to the baseline case is caused by the shorter recirculation length in the suction case. Downstream of $x/c = 1.1$, however, the agreement between numerical and experimental results is quite good.

Instantaneous gray-scale contours of the spanwise vorticity component for the suction case are presented in Fig. 13. Although the flow remains much closer to the body surface, the separated shear layer is still clearly visible in the region downstream of the separation point.

In addition to the potential causes mentioned earlier regarding the observed differences between numerical and experimental results, the modeling of the slot in the suction case might also be a contributing factor. As seen in Fig. 4, the width of the slot was increased to allow for adequate resolution of the gradients (there are approximately 17 grid points within the "slot"). This increased slot width can have an effect on the separation location as well as on the separation angle, although it seems more likely that other factors cause the discrepancies.

Finally, a comment should be made regarding the spanwise domain width of $\Delta Z/c = 0.142$. In a series of initial simulations (including the ones performed for the CFD Validation Workshop[3] in March 2004), the computational domain had a spanwise extent of $\Delta Z/c = 0.071$. Upon doubling the domain width to the present

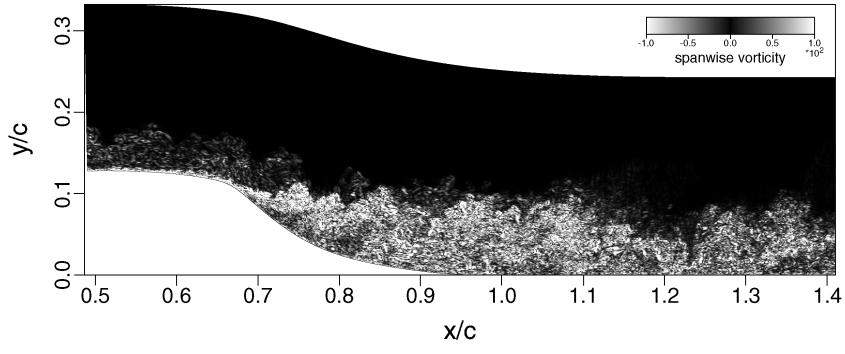

Fig. 13 Instantaneous gray-scale contours of the spanwise vorticity component: case with steady suction.

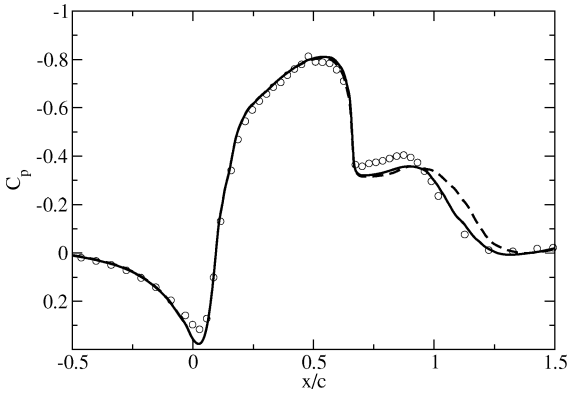

Fig. 14 Influence of the spanwise domain width on the surface-pressure coefficient, baseline case: – – –, $\Delta Z/c = 0.071$ and ——, $\Delta Z/c = 0.142$.

value (while keeping the same spanwise resolution, i.e., doubling the number of modes/collocation points), a significant improvement was obtained in the agreement between experiments and the DNS, especially for the baseline case. This improvement is illustrated in Fig. 14, where C_p distributions are shown for the simulation with $\Delta Z/c = 0.142$ in comparison to the case with $\Delta Z/c = 0.071$. For the narrow spanwise domain, the pressure recovery sets in noticeably later than in the experiments, and the predicted reattachment point is consequently located farther downstream ($x/c \approx 1.25$ vs $x/c \approx 1.19$ for $\Delta Z/c = 0.142$). Although the possibility exists that the present results are still not completely independent of the spanwise domain width, a further increase of $\Delta Z/c$ was not feasible with the available computational resources.

V. Conclusions

A high-order-accurate numerical method for the incompressible Navier–Stokes equations in curvilinear coordinates was presented and employed for simulating the turbulent flow over a wall-mounted hump. The primary purpose of the present investigation was to assess the feasibility of accurately predicting key quantities such as pressure distribution, mean flow statistics, and reattachment length for complex turbulent flows without the use of turbulence models. Although the present simulations were shown to not be fully resolved all of the way down to the smallest scales, good agreement with available experimental data was obtained. Potential causes for the overprediction of the reattachment length in both the baseline case and the case with steady suction were discussed, but more definitive answers can only be obtained by performing additional simulations and by obtaining measurements of the freestream turbulence characteristics of the NASA Langley Research Center shear flow tunnel in the hump model configuration.

The results obtained from the present coarse DNS are (at least) as good as the predictions obtained by other NASA workshop participants who employed various turbulence models for the investigation of the same flow. Taking into consideration that, with the rapidly increasing availability of powerful computers such as the Cray X1, turnaround times for DNS have decreased significantly (given that high-order-accurate, efficient Navier–Stokes solvers are employed), DNS is becoming a viable alternative to simulations using (sophisticated) turbulence models. Although DNS remains computationally more expensive, results obtained from such simulations provide true insight into the flow physics. Furthermore, DNS represents a true predictive tool, whereas most turbulence models have yet to be shown to have this capability. In other words, most turbulence models can be tuned to yield a desired result, but because such constants are generally not universal, they oftentimes have to be readjusted when the flow and/or the geometry changes. Lastly, DNS, much like experiments, can provide databases that are required for the development and validation of improved turbulence models.

Appendix: Coefficients in the Governing Equations

Vorticity-Transport Equations

$$cvta = \frac{1}{h_\xi^2 h_\eta}\frac{\partial h_\eta}{\partial \xi} - \frac{1}{h_\xi^3}\frac{\partial h_\xi}{\partial \xi}, \qquad cvtb = \frac{1}{h_\eta^2 h_\xi}\frac{\partial h_\xi}{\partial \eta} - \frac{1}{h_\eta^3}\frac{\partial h_\eta}{\partial \eta}$$

$$cvtc = \frac{1}{h_\xi h_\eta^2}\frac{\partial^2 h_\xi}{\partial \eta^2} + \frac{1}{h_\xi^2 h_\eta}\frac{\partial^2 h_\eta}{\partial \xi^2} - \frac{1}{h_\xi^2 h_\eta^2}\left[\left(\frac{\partial h_\xi}{\partial \eta}\right)^2 + \left(\frac{\partial h_\eta}{\partial \xi}\right)^2\right] - \frac{1}{h_\xi h_\eta^3}\left(\frac{\partial h_\xi}{\partial \eta}\frac{\partial h_\eta}{\partial \eta}\right) - \frac{1}{h_\xi^3 h_\eta}\left(\frac{\partial h_\xi}{\partial \xi}\frac{\partial h_\eta}{\partial \xi}\right)$$

$$cvtd = \frac{2}{h_\xi^2 h_\eta}\frac{\partial h_\xi}{\partial \eta}, \qquad cvte = \frac{-2}{h_\xi h_\eta^2}\frac{\partial h_\eta}{\partial \xi}$$

$$cvtf = \frac{1}{h_\xi^3 h_\eta^3}\left[h_\xi^2\frac{\partial h_\eta}{\partial \eta}\frac{\partial h_\eta}{\partial \xi} + h_\eta^2\left(h_\xi\frac{\partial^2 h_\xi}{\partial \xi \partial \eta} - \frac{\partial h_\xi}{\partial \xi}\frac{\partial h_\xi}{\partial \eta}\right) - h_\xi^2 h_\eta\frac{\partial^2 h_\eta}{\partial \xi \partial \eta}\right]$$

Velocity Equations

$$cpla_\xi = h_\xi^2, \qquad cplb_\xi = \frac{1}{h_\eta}\frac{\partial h_\eta}{\partial \xi} - \frac{1}{h_\xi}\frac{\partial h_\xi}{\partial \xi}$$

$$cplc_\xi = \frac{1}{h_\eta}\frac{\partial^2 h_\eta}{\partial \xi^2} - \frac{1}{h_\xi h_\eta^2}\frac{\partial h_\eta}{\partial \xi}\left(h_\eta\frac{\partial h_\xi}{\partial \xi} + h_\xi\frac{\partial h_\eta}{\partial \xi}\right)$$

$$cpra_\xi = -h_\xi^2$$

$$cprb_\xi = -\frac{1}{h_\eta}\frac{\partial^2 h_\xi}{\partial \xi \partial \eta} + \frac{1}{h_\xi h_\eta^2}\frac{\partial h_\xi}{\partial \eta}\left(h_\eta\frac{\partial h_\xi}{\partial \xi} + h_\xi\frac{\partial h_\eta}{\partial \xi}\right)$$

$$cprc_\xi = -\frac{1}{h_\eta}\frac{\partial h_\xi}{\partial \eta}, \qquad cprd_\xi = \frac{h_\xi}{h_\eta^2}\frac{\partial h_\eta}{\partial \xi}, \qquad cpre_\xi = -\frac{h_\xi}{h_\eta}$$

$$cpla_\eta = \frac{h_\xi^2}{h_\eta^2}, \qquad cplb_\eta = h_\xi^2, \qquad cplc_\eta = \frac{3}{h_\eta}\frac{\partial h_\eta}{\partial \xi} - \frac{1}{h_\xi}\frac{\partial h_\xi}{\partial \xi}$$

$$cpld_\eta = \frac{h_\xi}{h_\eta^2}\frac{\partial h_\xi}{\partial \eta} - \frac{h_\xi^2}{h_\eta^3}\frac{\partial h_\eta}{\partial \eta}$$

$$cple_\eta = \frac{h_\xi}{h_\eta^2}\frac{\partial^2 h_\xi}{\partial \eta^2} + \frac{1}{h_\eta}\frac{\partial^2 h_\eta}{\partial \xi^2} - \frac{h_\xi}{h_\eta^3}\frac{\partial h_\xi}{\partial \eta}\frac{\partial h_\eta}{\partial \eta} - \frac{1}{h_\xi h_\eta}\frac{\partial h_\xi}{\partial \xi}\frac{\partial h_\eta}{\partial \xi} + \frac{1}{h_\eta^2}\left[\left(\frac{\partial h_\eta}{\partial \xi}\right)^2 - \left(\frac{\partial h_\xi}{\partial \eta}\right)^2\right]$$

$$cpra_\eta = h_\xi^2, \qquad cprb_\eta = -h_\xi, \qquad cprc_\eta = -2\frac{h_\xi}{h_\eta}\frac{\partial h_\eta}{\partial \xi}$$

$$cprd_\eta = \frac{h_\xi}{h_\eta^3}\frac{\partial h_\eta}{\partial \eta}\frac{\partial h_\eta}{\partial \xi} - \frac{1}{h_\xi h_\eta}\left(\frac{\partial h_\xi}{\partial \eta}\frac{\partial h_\xi}{\partial \xi} - h_\xi\frac{\partial^2 h_\xi}{\partial \xi \partial \eta}\right) + \frac{1}{h_\eta^2}\left(2\frac{\partial h_\xi}{\partial \eta}\frac{\partial h_\eta}{\partial \xi} - h_\xi\frac{\partial^2 h_\eta}{\partial \xi \partial \eta}\right), \qquad cpre_\eta = \frac{2}{h_\eta}\frac{\partial h_\xi}{\partial \eta}$$

$$cpla_z = h_\xi^2, \qquad cplb_z = \frac{1}{h_\eta}\frac{\partial h_\eta}{\partial \xi} - \frac{1}{h_\xi}\frac{\partial h_\xi}{\partial \xi}, \qquad cpra_z = h_\xi$$

$$cprb_z = \frac{h_\xi}{h_\eta}\frac{\partial h_\eta}{\partial \xi}, \qquad cprc_z = -\frac{h_\xi}{h_\eta}\frac{\partial h_\xi}{\partial \eta}, \qquad cprd_z = -\frac{h_\xi^2}{h_\eta}$$

Wall-Vorticity Equations

$$cwla_\xi = h_\xi^2, \qquad cwlb_\xi = \frac{3}{h_\eta}\frac{\partial h_\eta}{\partial \xi} - \frac{1}{h_\xi}\frac{\partial h_\xi}{\partial \xi}$$

$$cwlc_\xi = \frac{1}{h_\eta}\frac{\partial^2 h_\eta}{\partial \xi^2} + \frac{1}{h_\eta^2}\left(\frac{\partial h_\eta}{\partial \xi}\right)^2 - \frac{1}{h_\xi h_\eta}\frac{\partial h_\xi}{\partial \xi}\frac{\partial h_\eta}{\partial \xi}$$

$$cwra_\xi = \frac{1}{h_\xi h_\eta}\frac{\partial h_\xi}{\partial \xi} - \frac{1}{h_\eta^2}\frac{\partial h_\eta}{\partial \xi}, \qquad cwrb_\xi = -\frac{1}{h_\eta}$$

Acknowledgments

This work was supported by the Air Force Office of Scientific Research under Grant F49620-02-1-0122, with Thomas J. Beutner serving as the Program Manager. Computing time on the Cray X1 at the Army High Performance Computing Research Center and the Arctic Region Supercomputing Center is gratefully acknowledged. Thanks also to Stefan Wernz for his helpful contributions.

References

[1]Liu, J. T. C., "Coherent Structures in Transitional and Turbulent Free Shear Flows," *Annual Review of Fluid Mechanics*, Vol. 21, 1989, pp. 285–315.

[2]Neumann, J., and Wengle, H., "Coherent Structures in Controlled Separated Flow over Sharp-Edged and Rounded Steps," *Journal of Turbulence*, Vol. 5, No. 22, 2004, pp. 1–24.

[3]Rumsey, C. L., Gatski, T. B., Sellers, W. L., III, Vatsa, V. N., and Viken, S. A., "Summary of the 2004 CFD Validation Workshop on Synthetic Jets and Turbulent Separation Control," AIAA Paper 2004-2217, June–July 2004.

[4]Seifert, A., and Pack, L. G., "Active Flow Separation Control on Wall-Mounted Hump at High Reynolds Numbers," *AIAA Journal*, Vol. 40, No. 7, 2002, pp. 1363–1372.

[5]Greenblatt, D., Paschal, K., Yao, C., Harris, J., Schaeffler, N., and Washburn, A., "A Separation Control CFD Validation Test Case Part 1: Baseline and Steady Suction," AIAA Paper, 2004-2220, June–July 2004.

[6]Greenblatt, D., Paschal, K., Yao, C., and Harris, J., "A Separation Control CFD Validation Test Case Part 2: Zero Efflux Oscillatory Blowing," AIAA Paper, 2005-0485, Jan. 2005.

[7]Moin, P., and Mahesh, K., "Direct Numerical Simulation: a Tool in Turbulence Research," *Annual Review of Fluid Mechanics*, Vol. 30, 1998, pp. 539–578.

[8]Manhart, M., and Friedrich, R., "DNS of a Turbulent Boundary Layer with Separation," *International Journal of Heat and Fluid Flow*, Vol. 23, No. 5, 2002, pp. 572–581.

[9]Skote, M., and Henningson, D. S., "Direct Numerical Simulation of a Separated Turbulent Boundary Layer," *Journal of Fluid Mechanics*, Vol. 471, 2002, pp. 107–136.

[10]Garg, V. K., *Applied Computational Fluid Dynamics*, Marcel Dekker, New York, 1998.

[11]Meitz, H., and Fasel, H. F., "A Compact-Difference Scheme for the Navier–Stokes Equations in Vorticity-Velocity Formulation," *Journal of Computational Physics*, Vol. 157, No. 1, 2000, pp. 371–403.

[12]Lele, S. K., "Compact Finite Difference Schemes with Spectral-Like Resolution," *Journal of Computational Physics*, Vol. 103, No. 1, 1992, pp. 16–42.

[13]Ferziger, J. H., *Numerical Methods for Engineering Application*, 2nd ed., Wiley, New York, 1998.

[14]Dennis, C. R., and Hudson, J. D., "Compact h^4 Finite-Difference Approximations to Operators of Navier–Stokes Type," *Journal of Computational Physics*, Vol. 85, No. 2, 1989, pp. 390–416.

[15]Bandy, V. A., "Black Box Multigrid for Convection-Diffusion Equations on Advanced Computers," Ph.D. Dissertation, Dept. of Mathematics, Univ. of Colorado, Denver, CO, 1996.

[16]Briggs, B., *A Multigrid Tutorial*, Society for Industrial and Applied Mathematics, Philadelphia, 1987.

[17]Meitz, H., "Numerical Investigation of Suction in a Transitional Flat-Plate Boundary Layer," Ph.D. Dissertation, Dept. of Aerospace and Mechanical Engineering, Univ. of Arizona, Tucson, AZ, 1996.

[18]Duraiswami, R., and Prosperetti, A., "Orthogonal Mapping in Two Dimensions," *Journal of Computational Physics*, Vol. 98, No. 2, 1992, pp. 254–268.

[19]Wernz, S., Valsecchi, P., Gross, A., and Fasel, H. F., "Numerical Investigation of Turbulent Wall Jets over a Convex Surface," AIAA Paper 2003-3727, June 2003.

C. Rumsey
Guest Editor